Observations of tracer ventilation in the Cape Basin, Agulhas Current Retroflection

Renske Koets[1], Sebastiaan Swart[1,2], Kathleen Donohue[3], and Marcel du Plessis[1]

[1]Department of Marine Sciences, University of Gothenburg, Sweden
[2]Department of Oceanography, University of Cape Town, Rondebosch, South Africa
[3]Graduate School of Oceanography, University of Rhode Island, USA

Correspondence: Renske Koets (renske.koets@gmail.com)

Abstract. The Cape Basin is a highly dynamic region, strongly influenced by the Agulhas Retroflection and its associated ring shedding. The region is characterized by high eddy kinetic energy, amplified mixing and water mass transformation. While model studies have shown that meso- to submesoscale features enhance water mass formation and tracer stirring, there has been limited observations made at the required spatiotemporal scales to capture such stirring and mixing processes. This study integrates high-resolution glider observations with satellite data to indicate the presence of shear-driven instabilities occurring at submesoscale fronts that enhance vertical diapycnal transport, leading to low apparent oxygen utilization and high levels of particulate organic carbon in the deeper ocean. These tracers are then distributed within the ocean interior via mesoscale advection and stirring along isopycnals, providing observational evidence for the role of the meso- to submesoscale strain field in surface to ocean interior water mass transformation and their broader implications on ocean circulation.

1 Introduction

The Agulhas Current is a key component of the global ocean circulation, facilitating the exchange of heat and salt between the Indian and Atlantic Ocean (Beal et al., 2011). Following the eastern coastline of South Africa, the current reaches the southern tip of the continent, where it changes direction and loops back into the Indian Ocean as the Agulhas Return Current - known as the Retroflection. At the Retroflection, a portion of the Agulhas Current sheds off and 'leaks' into the Atlantic Ocean. The shedding of Agulhas eddies, rings and filaments bring the warm, saline waters from the Indian Ocean into the cooler, fresher waters of the Atlantic Ocean. The Agulhas leakage provides a pathway for warm and salty waters to enter the Atlantic Ocean, contributing to the Atlantic Meridional Overturning Circulation (AMOC), making this region important for the global climate (Rühs et al., 2022).

The interaction of the Agulhas Current with regional topography generates meanders and mesoscale features that contribute to elevated eddy kinetic energy (EKE). These EKE values are comparable to those found in western boundary extensions and hot spots of the ACC, where strong mesoscale dynamics enhance mixing and ventilation by facilitating tracer exchange between the surface and interior ocean (Dove et al., 2022). Regions of high EKE and strong mesoscale activity often coincide with enhanced strain fields and frontal structures (Bettencourt et al., 2015). To identify these regions of high strain, the Finite-Size

Lyapunov Exponent (FSLE) is used as a Lagrangian diagnostic to locate where water parcels converge or diverge, marking transport barriers and pathways for tracer dispersion in the ocean (d'Ovidio et al., 2004).

A key region where these dynamics are particularly pronounced is the Agulhas Retroflection, which is characterized by strong temperature gradients and elevated EKE, closely aligned with sharp frontal structures, as indicated by high FSLE values (Fig. 1). These energetic mesoscale features are expected to play an important role in ventilation and water mass transformation (Penven et al., 2006). Yet, directly observing the fine-scale mechanisms driving ventilation and tracer transport remains challenging due to the high spatial and temporal resolution required to resolve such processes.

Ventilation in the Cape Basin is likely driven by a spectrum of flow regimes, ranging from quasi-geostrophic flows with low Rossby numbers that primarily induce isopycnal stirring along density surfaces, to more turbulent flows with high Rossby numbers that promote vertical mixing (Boebel et al., 2003). Submesoscale flows, with small horizontal and vertical scales (< 10 km), play a key role in these processes, enhancing both lateral and vertical transport of tracers to depth (Yu et al., 2024). These small-scale flows arise from interactions such as mesoscale eddies (Roullet et al., 2012) and submesoscale fronts (Omand et al., 2015; Siegelman et al., 2020), driving mixed layer baroclinic instabilities (Callies and Ferrari, 2018), often associated with strong vertical velocities. In addition, shear instabilities, which result from strong vertical gradients in the horizontal velocity, can further contribute to diapycnal mixing, facilitating the vertical transport of tracers across density layers (Tu et al., 2024). These processes provide important pathways for tracer transport across the pycnocline, contributing to ventilation (Pham et al., 2024).

Observations in the Southern and Atlantic Oceans have shown that enhanced ventilation is associated with reduced apparent oxygen utilization (AOU) values at depths far below the mixed layer (Dove et al., 2022; Balwada et al., 2024; Liu and Tanhua, 2024). Low AOU values – those with recent contact with the atmosphere – at depths far removed from the surface suggest the existence of vertical pathways through which surface waters can be transported to deep layers, as respiration in the ocean interior acts as an oxygen sink (Dove et al., 2021). Given its reliability as a tracer for ventilation, AOU is used in this study to quantify the vertical and lateral transport in the Cape Basin.

The strong vertical velocities arising from submesoscale flows, not only facilitate the transport of dissolved oxygen but also influence the vertical redistribution of particles, with shifts in particle size distribution and an enhancement of the vertical movement of particulate organic carbon (POC) across the base of the ocean's euphotic zone (Chen and Schofield, 2024). Previous studies suggest that carbon flux is not solely driven by the gravitational sinking of organic matter but is also influenced by physical processes, such as advection and stirring, which transport organic matter to deeper layers of the ocean (Boyd et al., 2019; Omand et al., 2015; Lévy et al., 2012; Chen and Schofield, 2024). This vertical redistribution of POC plays a crucial role in the ocean's biological pump, directly impacting the global carbon cycle. By sequestering carbon in the deep ocean, POC transport is an essential component in regulating the atmospheric CO_2 concentrations (Kwon et al., 2009). Understanding the
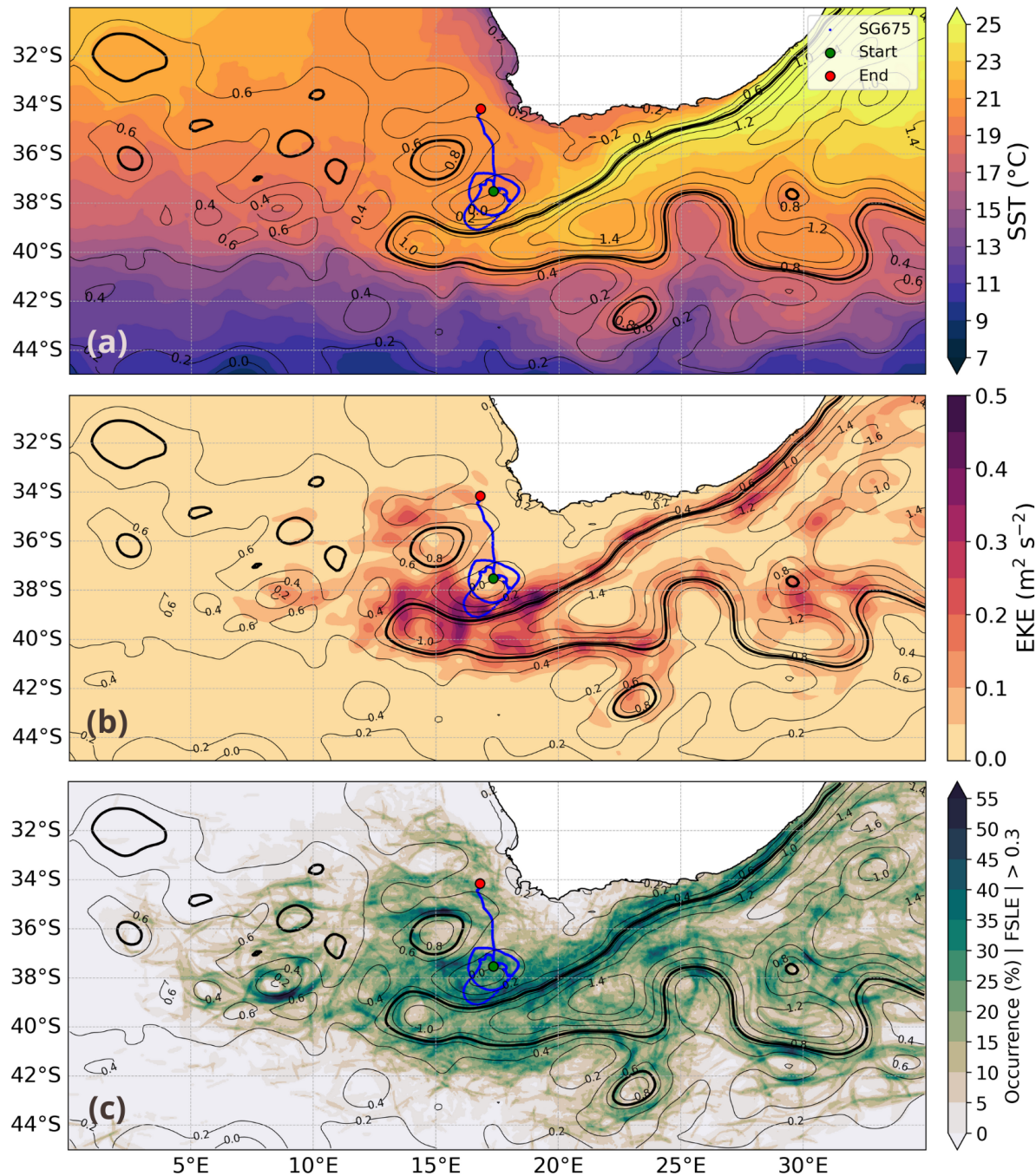
Figure 1. (a) Sea Surface Temperature (SST), (b) Eddy Kinetic Energy (EKE), and (c) Occurence of Finite-Size Lyapunov Exponent (FSLE) > 0.3, averaged over the glider deployment (22 March to 23 May 2023). Seaglider trajectory is shown in blue. Green and red dots mark the start and end of the glider mission. Contours indicate Absolute Dynamic Topography (ADT, dyn m), with the thick black line (0.7 dyn m) representing the core of the Agulhas Current, Retroflection, and Rings.

60 processes related to the vertical flux of POC is essential for predicting how the biological pump might respond to a changing climate.

Despite the recognized importance of ventilation, the fine-scale processes governing the exchanges remain poorly observed, and the potential role of ventilation in the Agulhas system is not well understood. To address these knowledge gaps, this study uses

65 high-resolution tracer observations, collected from an underwater glider, deployed during the QUantifying Interocean fluxes in the Cape Cauldron Hotspot of Eddy kinetic energy (QUICCHE) field campaign. Glider-observed physical and biogeochemical variables provide valuable insight into the distribution and intensity of ventilation events occurring in this high EKE region of the Cape Basin.

2 Methods

70 ### 2.1 Glider observations and data processing

An underwater glider (Seaglider - SG675) was deployed between March 22 to May 23, 2023 (63 days) within the Cape Basin, SW of South Africa. The glider sampled between the surface and a 1000 m depth, completing 297 profiles and covering a distance of approximately 1650 km (Fig. 1). The Seaglider was equipped with an unpumped Seabird CT sensor that measured conductivity, temperature, and pressure, an Aanderaa optode 4831 that measured oxygen and Wet Labs ECO puck that mea-

75 sured Chl-a and backscatter at 470 and 700 nm.

To ensure data quality, conservative temperature and salinity outliers were removed using the wrapper function in GliderTools (Gregor et al., 2019). Within this function, any detected spikes were eliminated using a 5-point rolling median and subsequently smoothed with a Savitzky-Golay filter. Raw data was corrected for sensor thermal-lag using the IOP basestation code that

80 applied a first-order thermistor-response lag (Garau et al., 2011). The remaining thermal lag in the final dataset was found negligible, as the absolute difference between the mean of all climbs and dives in conservative temperature and absolute salinity at the thermocline was 0.04 °C and 0.015 g kg^{-1}, respectively. Part of the climb–dive differences may also reflect spatial variability, especially in strong frontal regions. The mixed layer depth (MLD) is defined as the depth z at which the difference in potential density referenced to the potential density at 10 m first exceeds a threshold value of 0.03 kg m^{-3}

85 (de Boyer Montégut et al., 2004).

2.2 Oxygen observations and deriving AOU

Oxygen is measured by the glider with an Aanderaa Optode 4831. The oxygen dataset is smoothed using a Savitzky-Golay filter with a 2nd order polynomial. The ship CTD is used to calibrate the glider's oxygen measurements during deployment. An offset of 22.28 μm kg^{-1} is added to the glider's oxygen concentration along the transect.

90

AOU is calculated:

$$AOU = [O_2\ solubility] - [O_2\ observed] \tag{1}$$

where $[O_2\ solubility]$ represents the solubility of oxygen in seawater and $[O_2\ observed]$ the observed oxygen concentration measured with the Oxygen Optode 4831. The $[O_2\ solubility]$ represents the amount of oxygen that can dissolve in a given volume of seawater depending on temperature, pressure and salinity and is calculated with TEOS-10 (http://www.teos-10.org/).

2.3 Mapping and grid resolution

The glider data were mapped onto a regular grid with a vertical resolution of 0.5 m and onto a horizontal resolution of 1.5 km. To account for the spatial variability discussed in Sec. 2.1 and to minimize the effect of glider advection, distance was calculated relative to the surrounding current. From this point onward, this will be referred to as "distance". After this correction, the cumulative distance was reduced to approximately half of the along-track distance.

This distance is derived using the horizontal speed of the glider obtained by the Glide Slope Model (GSM) (Bennett et al., 2021) and calculated by averaging the horizontal speed of two consecutive glider measurements and multiplying the result by the time interval, Δt. While Δt was nominally 5 seconds, occasional clock resets introduced variability. To maintain consistency, Δt was assumed to be 5 seconds for the calculations. The GSM-derived distance differed by 3.55% from the distance obtained using the horizontal speed from the Hydrodynamical Model. Both time and glider positions were interpolated to the horizontal distance grid.

2.4 Other glider derived variables

2.4.1 Backscatter and derived POC

Optical backscatter at two wavelengths, 470 nm and 700 nm, was measured using Wet Labs sensors. Raw backscatter data, provided in counts, were processed into total backscatter (bbp) using GliderTools processing (Gregor et al., 2019). This processing tool is used to remove profiles with high backscatter values below 300 m depth. Subsequently raw sensor counts were calibrated using the manufacturer-provided scale factors and dark counts. Total backscatter was then calculated following the method described by Zhang et al. (2009) and despiked using a 7-point rolling mean filter (Briggs et al., 2011). The backscatter spectral slope ($\gamma_{b_{bp}}$) was calculated from the despiked backscatter at the two wavelengths following:

$$b_{bp}(\lambda) = b_{bp}(\lambda_0)\left(\left(\frac{\lambda}{\lambda_0}\right)\right)^{\gamma_{b_{bp}}}. \tag{2}$$

Field studies have indicated a trend of an increase in the spectral slope of back scattering γ with an increase in relative contribution of small-sized particles to the total particle concentration (Reynolds et al., 2001). We use the backscatter slope to

qualitatively determine the relative composition of small to large particles below the mixed layer to infer regions of enhanced ventilation.

The total backscatter at 700 nm (bbp700) is used to estimate large, fast-sinking and small, slow-sinking POC with empirical factors of 37,537 mg C m^{-2} in the mixed layer and 31,519 mg C m^{-2} below (Wang and Fennel, 2023). This approach assumes a constant bbp700-POC relationship across different regions and negligible effects of plankton decomposition, except for a shift in particle composition between the mixed layer and the deeper ocean (Lacour et al., 2019).

2.4.2 Instabilities

Instabilities are characterized by weak vertical stratification N^2 and an enhancement of the vertical shear $\frac{\partial u}{\partial z}$. To assess these instabilities, the geostrophic vertical shear is calculated from the thermal wind balance as

$$S_z = \frac{1}{f} b_x, \tag{3}$$

where $f = 2\Omega \sin\varphi$ and $b_x = \frac{\partial b}{\partial x}$ is the partial derivative of buoyancy in distance, with $\partial x = 1.5$ km (Bernat, 2024).

The interplay between vertical shear and stratification can be quantified using the Richardson number Ri, which indicates the tendency for shear-driven turbulence to develop.

$$Ri = \frac{N^2 f^2}{b_x}. \tag{4}$$

Abarbanel et al. (1984) defined stratified shear flow as stable for $Ri > 1$, weakly unstable for $0.25 < Ri < 1$, and unstable for $Ri < 0.25$, where turbulence develops as shear overcomes stratification (Ruan et al., 2017).

2.4.3 Geostrophic velocity

The geostrophic velocity $\mathbf{u_g}$ is given by

$$\mathbf{u_g} = \frac{g}{f} \hat{k} \times \nabla\phi, \tag{5}$$

where the dynamic height anomaly ϕ with respect to the surface at a reference pressure of $p_{ref} = 0$ is determined from glider data using the TEOS-10 function `gsw.geostrophy.geo_strf_dyn_height`. The geostrophic velocity is referenced with the bottom profile and smoothed with a 15 point rolling mean and a Gaussian filter.

2.4.4 Spiciness

Spiciness τ is defined through its differential as

$$d\tau = \rho(\alpha d\theta + \beta dS), \tag{6}$$

where θ is the Conservative Temperature (°C), S is the Absolute Salinity (g kg^{-1}), ρ is the potential density (kg m^{-3}) referenced with the surface and

$$\alpha = -\frac{1}{\rho}\frac{\partial \rho}{\partial \theta}, \quad \beta = \frac{1}{\rho}\frac{\partial \rho}{\partial S}$$

150 represent, respectively, the thermal expansion coefficient (K^{-1}) and the saline contraction coefficient (g^{-1} kg) (Shcherbina et al., 2009). A mirror-padded Blackman low-pass filter with a half-width of 0.08 kg m^{-3} (41 grid points) is used to improve the signal-to-noise ratio.

2.5 Satellite products and FSLE

To identify surface-level events that may influence ventilation processes, we have analyzed the Sea Level Anomaly (SLA),
155 from AVISO, with a 0.125° resolution and the Sea Surface Temperature obtained from the Global SST and Sea Ice Analysis, L4 OSTIA, 0.05° daily. Where the SLA is estimated by merging L3 along-track measurements from various altimeter missions.

Eddy kinetic energy (EKE) is calculated using the geostrophic velocities from the AVISO product.

$$EKE = \frac{1}{2}(u'^2 + v'^2), \tag{7}$$

160 where u' and v' are the deviations from the mean $(\bar{u}, \bar{v})$ (Richardson, 1983).
Ageostrophic motions at fronts can be indicated by an increased FSLE (Guo et al., 2024). The FSLE is defined as the inverse time of separation of two particles from their initial distance δ_0 to a final distance δ_f (d'Ovidio et al., 2004). The particles are advected by altimetry-derived velocities and their trajectories are computed by forward-time λ^+ and backward-time λ^- integration of the altimetry velocities. Large timescales of separation of the particles λ^- indicates an intense strain field (Siegelman
165 et al., 2020). The separation's growth rate FSLE is defined as:

$$\lambda^+ = \frac{1}{\tau}\ln\left(\frac{\delta_f}{\delta_0}\right); \tag{8}$$

$$\lambda^- = -\frac{1}{\tau}\ln\left(\frac{\delta_f}{\delta_0}\right); \tag{9}$$

where δ_0 is the initial distance between a particle at (x,y,t) and its four closest neighbors. δ_0 corresponds to the spatial resolution of the FSLE grid. δ_f is the final distance between particles. τ is the minimum time (among the 4 particle pairs) to reach

the distance δ_f (Sudre et al., 2023). FSLE is calculated following the method of d'Ovidio et al. (2004), using $\tau = 7$ days, $\delta_0 = 0.05°$ ($\sim 6\,\mathrm{km}$) and $\delta_f = 0.5°$ ($\sim 56\,\mathrm{km}$). The initial separation δ_0 is set close to the altimetry grid spacing ($\frac{1}{8}°$) and smaller than the regional first-baroclinic Rossby radius (~ 25 km) (Dudley B et al., 1998) to resolve meso- to submesoscale frontal features. The final separation δ_f is set so that $\delta_f = 10\delta_0$ following the method of Sudre et al. (2023). This choice ensures that FSLE captures the growth of submesoscale frontal features into larger mesoscale structures, representing the overall strain field. The time integral τ is chosen to align with typical mesoscale mixing timescales observed in the Cape Basin (Kersalé, M. et al., 2018; Capuano et al., 2018). The chosen parameters represent the lower limits permitted by the resolution of altimetry, bringing the FSLE fields closer to glider-scale observations. Parameter sensitivity tests indicate that further reductions in τ or δ_0 predominantly enhance noise rather than reveal additional coherent structures. Maximum values of the λ^+ and λ^- fields identify divergent and convergent flows, respectively (Berta et al., 2022). In particular, intersections of intense converging and diverging FSLE lines identify Lagrangian hyperbolic points, where particles and tracers are simultaneously being stretched along one direction and compressed along the other direction (d'Ovidio et al., 2004).

3 Results

3.1 Glider-observed ventilation events

During the deployment, the glider navigated in the Cape Basin, north of the Agulhas Retroflection. The glider's trajectory was significantly influenced by strong currents in the vicinity of a cyclonic eddy located around 18°E and 38°S. In general, this region is also influenced by filaments and anticyclonic eddies (Agulhas Rings) shedding off from the Agulhas Current, introducing warm and saline Indian Ocean waters into the South Atlantic, resulting in elevated SST (Fig. 1a). Using water-mass classification, the glider's observations reveal that these Indian Ocean waters (absolute salinity $S_a = 35.5$ g kg^{-1}; conservative temperature $CT = 16\,°\mathrm{C}$) are not confined to the surface layers and can be transported along isopycnals to depths of 250 m (Fig. 2). In the subsurface (50 - 200 m), they interact with South Atlantic waters ($S_a = 34.7$ g kg^{-1}, $CT = 13\,°\mathrm{C}$), highlighting the role of mesoscale eddies in stirring and redistributing heat and salinity. The strong differences in temperature (T) and salinity (S) between these water masses create strong horizontal T and S gradients, particularly between 550–620 km and 700–750 km along the glider's track (Fig. 2a, b). These thermohaline gradients influence stratification and may further drive isopycnal stirring and shear-induced mixing in the subsurface layers.

At intermediate depths (500 - 700 m), the glider reveals waters of Subantarctic origin with characteristics of Antarctic Intermediate Water (AAIW, $S_a < 34.6$ g kg^{-1} (Fu et al., 2019)), identified by its salinity minimum. These waters originate north of the Subantarctic Front, where strong wintertime convection ventilates the ocean, allowing AAIW to equilibrate with the atmosphere and become enriched with oxygen before it subducts (Xia et al., 2022). Once subducted, this recently ventilated AAIW is advected into the Cape Basin, where it flows beneath the warmer, saltier Agulhas waters and interacts with Agulhas Rings and filaments, which trap and stir the AAIW water masses, and maintaining elevated oxygen levels at intermediate depths (Giulivi and Gordon, 2006). The layering of different watermasses in the Cape Basin is evident in the glider obser-

vations (Fig. 2a, b), and when combined with mesoscale stirring, generates interleaving structures that can lead to enhanced lateral mixing (Schmid et al., 2003). This lateral mixing, combined with mesoscale eddy activity, redistributes oxygen-rich water masses and facilitates the vertical exchange across density layers. This is evident in the glider AOU profiles (Fig. 2c), where the distribution of oxygen is closely associated with interleaving signals in the T and S properties. When ventilation is limited, AOU is expected to increase with depth, indicating prolonged isolation from the surface, during which oxygen is consumed by respiration and other biological processes (Ito et al., 2004). This pattern is not consistently observed across the entire glider section. For instance, at approximately 380, 600, and 780 km along the glider's track, low AOU values – that has recently been at the surface – are observed to extend from the surface down to 700 m depth, indicating a well-ventilated region (Fig. 2c, black dashed lines and arrows). As these locations align with low-salinity patches at intermediate depths (Fig. 2b), they likely correspond to recently ventilated AAIW. In contrast to this broader ventilation pattern, a more localized ventilation event is observed at approximately 80 km along the glider's track, where low AOU values (50 μmol kg^{-1}) extend to 400 m depth over a horizontal distance of only 10 km. This suggests that the isopycnal transport of oxygen-rich waters at this location may result from a small-scale subsurface-intensified eddy or the glider is advected across a narrow filament of distinct water properties.

3.2   Linking lateral gradients to subduction

We contextualise the ventilation signatures in Fig. 2 by comparing the glider-measured lateral buoyancy gradients with altimetry-derived FSLE, which demonstrates the mesoscale circulation patterns in Fig. 1. The interaction between mesoscale eddies can drive horizontal strain, leading to the deformation of pre-existing buoyancy gradients and thereby intensify fronts through frontogenesis (Siegelman et al., 2020). These fronts can become unstable, leading to stronger mixing and enhanced vertical motions. These processes are often associated with baroclinic instabilities, where the density gradients between water masses drive vertical motions and intensify mixing responsible for the vertical transport of tracers (Siegelman et al., 2020). FSLE can be used as an indicator of the horizontal strain developing at fronts, with elevated values highlighting regions of intensified vertical motions and frontal instabilities.

Satellite altimetry observations reveal maximum diverging FSLE reaching over 2 day^{-1} (Fig. 3) at 405, 465 and 620 km along the glider's track, indicative of strong frontal structures. At 405 km, this enhanced FSLE coincides with increased horizontal buoyancy gradients observed by the glider between 300-700 m (Fig. 2d), the depth range associated with ventilation and re-newal of intermediate water (Fu et al., 2019). Localized FSLE peaks are observed to coincide with tracer subduction, as seen at 400 km along the glider's track, where pronounced salinity, temperature and AOU gradients indicate vertical transport of tracers reaching 700 m in depth (Fig. 2a–c). This aligns with the findings of (Bettencourt et al., 2015), which demonstrate that enhanced frontal activity from localized strain fields can generate strong tracer gradients at depth.
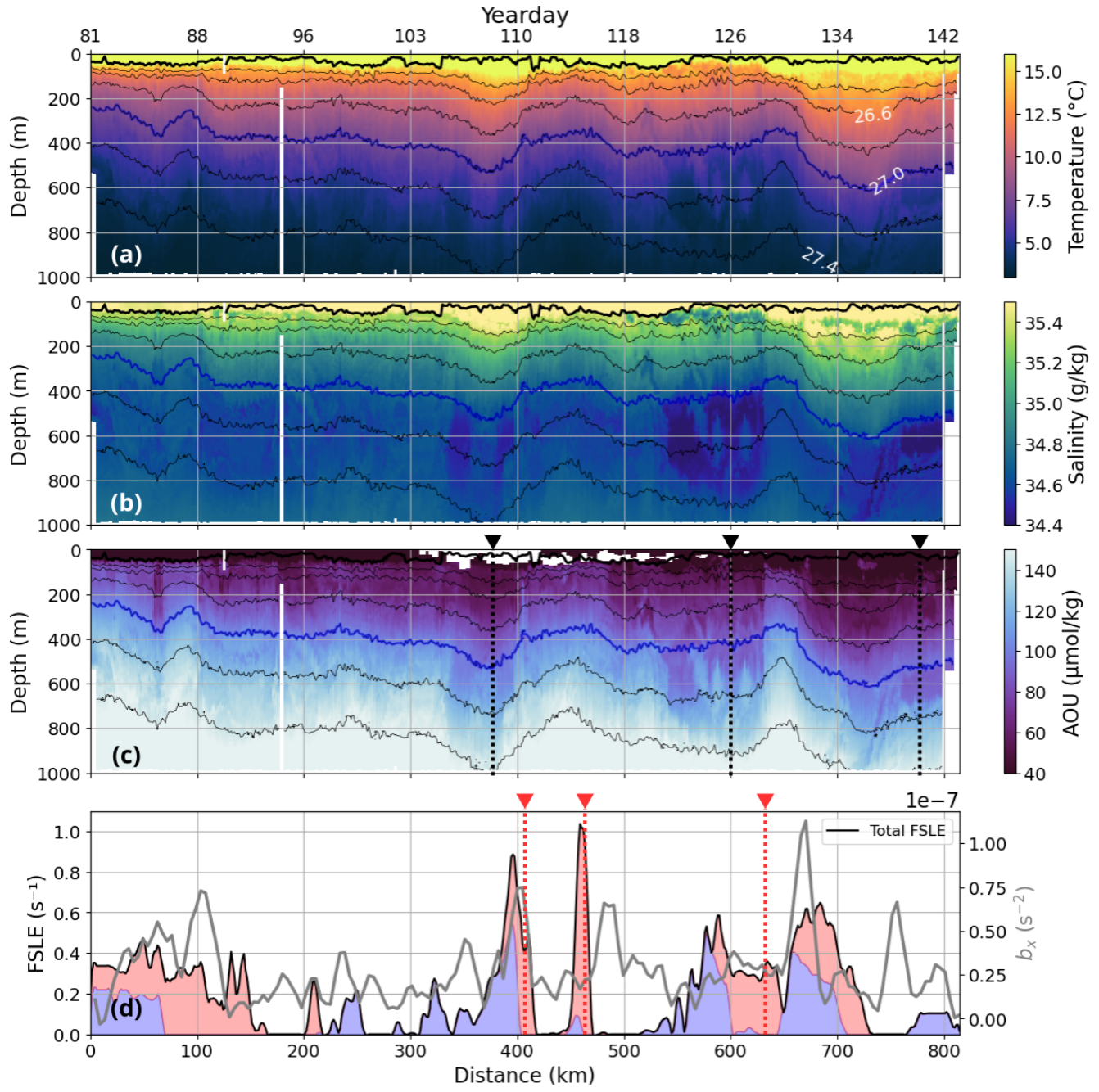
Figure 2. Glider sections showing (a) conservative temperature, (b) absolute salinity and (c) AOU. The black dashed lines and arrows indicate instances of low AOU at depths down to 700m. Isopycnals are overlaid using thin black contours, the 27 kg m^{-3} isopycnal is highlighted with a thick blue line and the MLD is depicted with the thick black line. (d) Averaged FSLE over a 0.125-degree radius around the gliders position, composed of diverging FSLE (red) stacked onto the converging FSLE (blue). The horizontal buoyancy gradient (b_x) is averaged between 300 – 700 m depth and shown in the gray line. The red dashed lines and arrows indicate yeardays corresponding to the satellite images of FSLE in Fig. 3.
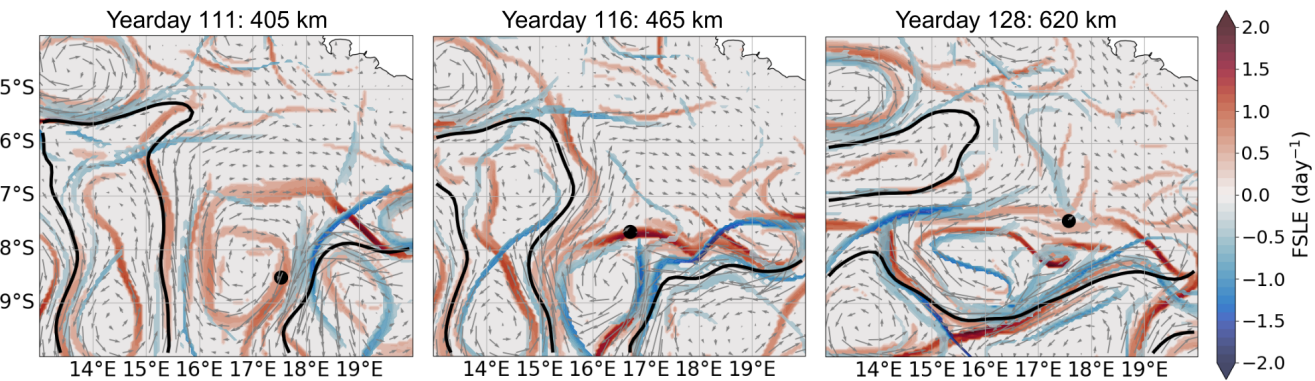
Figure 3. Maps of altimetry-derived FSLE during the glider deployment. The location of the glider is depicted with a black dot. Geostrophic velocities are represented using the gray vectors. The 0.7 dyn m SSH contour in black represents the core of the Agulhas Current, Retroflection and its associated Rings.

The pronounced FSLE peaks do not always coincide with strong horizontal buoyancy gradients observed by the glider - for example at 465 km in distance (Fig. 2d). Although the FSLE parameters were chosen at the lower limits permitted by altimetry to better approach glider scales (Sec. 2.5), the temporal and spatial resolution the FSLE field remain coarser than the glider resolution. As a result, it may not fully resolve sharper, short-term frontal structures observed by the glider or capture imme-
240 diate short-term surface dynamics. Additionally, surface dynamics may take time to propagate to depth, creating a temporal lag in the events visible at depth. Furthermore, the horizontal buoyancy gradients derived from the glider are likely underestimated, as the glider is largely advected with the background current and does not always cross ocean fronts perpendicularly. A full quantification of cross-frontal gradients requires sampling orthogonal to the front, and oblique sampling can lead to an underestimation of up to 50–70% (Thompson et al., 2016; du Plessis et al., 2019; Swart et al., 2020; Patmore et al., 2024). To
245 partially account for this effect, the distance covered by the glider is adjusted using the Glider Slope Model, as described in Sec. 2.3. Nevertheless the current calculation does not account for the full cross-frontal buoyancy gradient, potentially leading to an underestimation of its magnitude in regions where fronts are sampled at an oblique angle.

Assessing the regional significance of these localized processes can be done by considering the broader circulation of the Cape
250 Basin. The highest strain fields are observed at the Agulhas Retroflection, indicating strong mesoscale activity in this region (Fig. 1). The strong and highly variable strain field in the region of 38°S and 18°E coincides with elevated EKE, indicative of intensified mesoscale turbulence. This suggests that mesoscale instabilities play a key role in driving transport to depth across the Agulhas Retroflection, highlighting how localized strain fields, such as those observed along the glider's track, contribute to larger-scale ventilation and tracer subduction pathways across the Cape Basin.

255

Vertical velocities were derived from the Omega equation (Siegelman et al., 2020), using boundary conditions following (Leif N and Joyce M, 2010). Methods and results are provided in the Supplementary information. Strong vertical velocities $\mathcal{O}(100 \text{ m day}^{-1})$ are generally found in regions with elevated horizontal buoyancy gradients and high Rossby numbers, suggesting the role of submesoscale eddies in tracer subduction (Fig. S1). These enhanced vertical velocities often coincide with elevated

260 FSLE and low AOU at depths, however this alignment is not consistent throughout the glider section. The glider observations were often orientated along-front rather than cross-front, limiting the accuracy of derivatives such as $\partial u_g / \partial x$ and $\partial b / \partial x$. Consequently, the calculated vertical velocities are subject to large uncertainties, and the available estimates should be considered indicative rather than quantitative.

3.3 Linking particle size distribution to surface-interior exchange

265 To understand the role of meso- to submesoscale processes on the vertical and horizontal transport of tracers, we focus on a specific subset of the glider transect, spanning 600 to 720 km (yearday 126 to 136) along the glider's track. This period of the glider's trajectory was characterized by intense horizontal buoyancy gradients or fronts, where enhanced subsurface ventilation of AOU was observed. The vertical velocities in Fig. S2, show an alternating pattern indicative of a secondary circulation driven by frontogenesis, with the strongest downwelling roughly aligned with a strong POC subduction event near 650 km in

270 distance along the glider's track (Fig. 4). Within this transect the MLD exhibits more variability (Fig. 5), deepening initially, then shoaling, and deepening again. The lower rates of stratification within the pycnocline beneath the MLD (< 50 m) between 600 and 630 km along the glider's track (Fig. 5a) provides favorable conditions for the exchange of tracers between the surface boundary layer to the deeper ocean interior. Accordingly, the glider observations in Fig. 4 reveal that AOU, backscatter slope ($\gamma_{b_{bp}}$), and POC are primarily confined to the mixed layer, yet between 630 km to 670 km, diapycnal exchange occurs to

275 about 500 m depth, where they are then advected along sloping isopycnals between 630 km and 710 km to reach deeper waters.

To explain the diapycnal exchange from the mixed layer to deeper layers, we examine a stratified (3×10^{-4} s^{-2}) layer between 630 and 660 km along the glider's track at 80 m depth that is surrounded with elevated vertical shear (Fig. 5b), suggesting that this region could be prone to growing shear instabilities. This is reinforced by a peak in FSLE at 630 km (Fig. 2d) and yearday

280 128 (Fig 3), indicating the presence of an ocean front, that promotes enhanced mixing (Freilich and Mahadevan, 2021). Synonymously, Richardson numbers below 10 (red contour in Fig. 5c) suggest a transitional regime where stratification weakens, allowing shear instabilities to grow, that could be responsible for driving cross-isopycnal mixing (Tu et al., 2024).

The downward mixing across isopycnal is supported by the presence of elevated spiciness values observed between 630 and

285 660 km along the glider's track in Fig. 6c, indicative of warm, salty water, that is transported across the pycnocline spanning density layers 25.7 to 26.5 kg m^{-3} (Wang et al., 2022). AOU exhibits a similar pattern between 630 and 660 km, suggesting enhanced turbulence and vertical mixing between density layers 25.7 to 26.5 kg m^{-3}. The observed elevated vertical shear in the presence of the ocean front at 630 and 660 km along the glider's track suggests conditions favorable for generating turbulent mixing of POC across the pycnocline, further enhancing the redistribution of tracers and particles in the upper 400
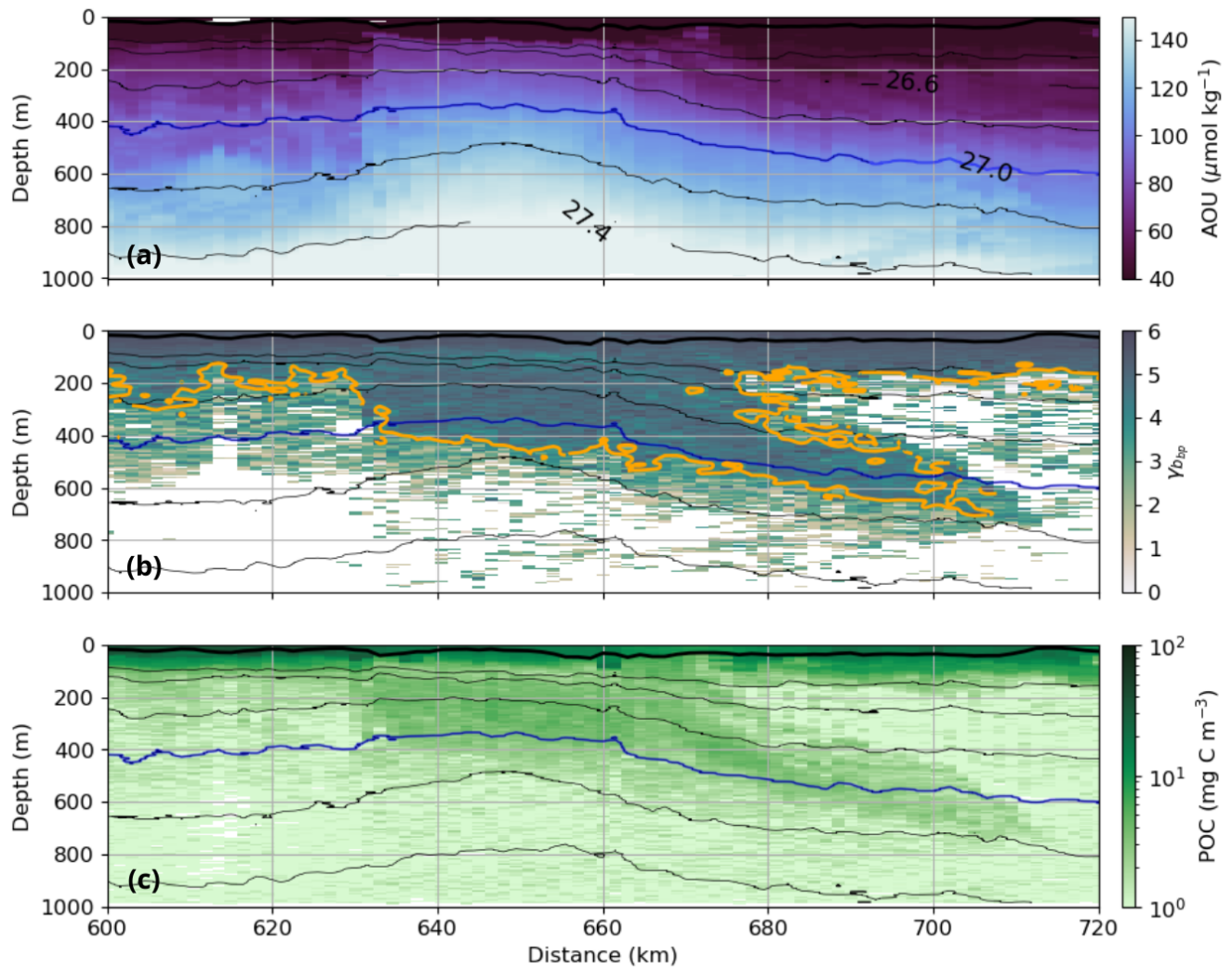
Figure 4. Subset of the glider timeseries showing (a) AOU, (b) spectral slope, where the yellow contour line indicates a spectral slope equal to 4 and (c) POC. Isopycnals are overlaid using thin black contours, the 27 kg m^{-3} isopycnal is highlighted with a thick blue line and the MLD is depicted with the thick black line.
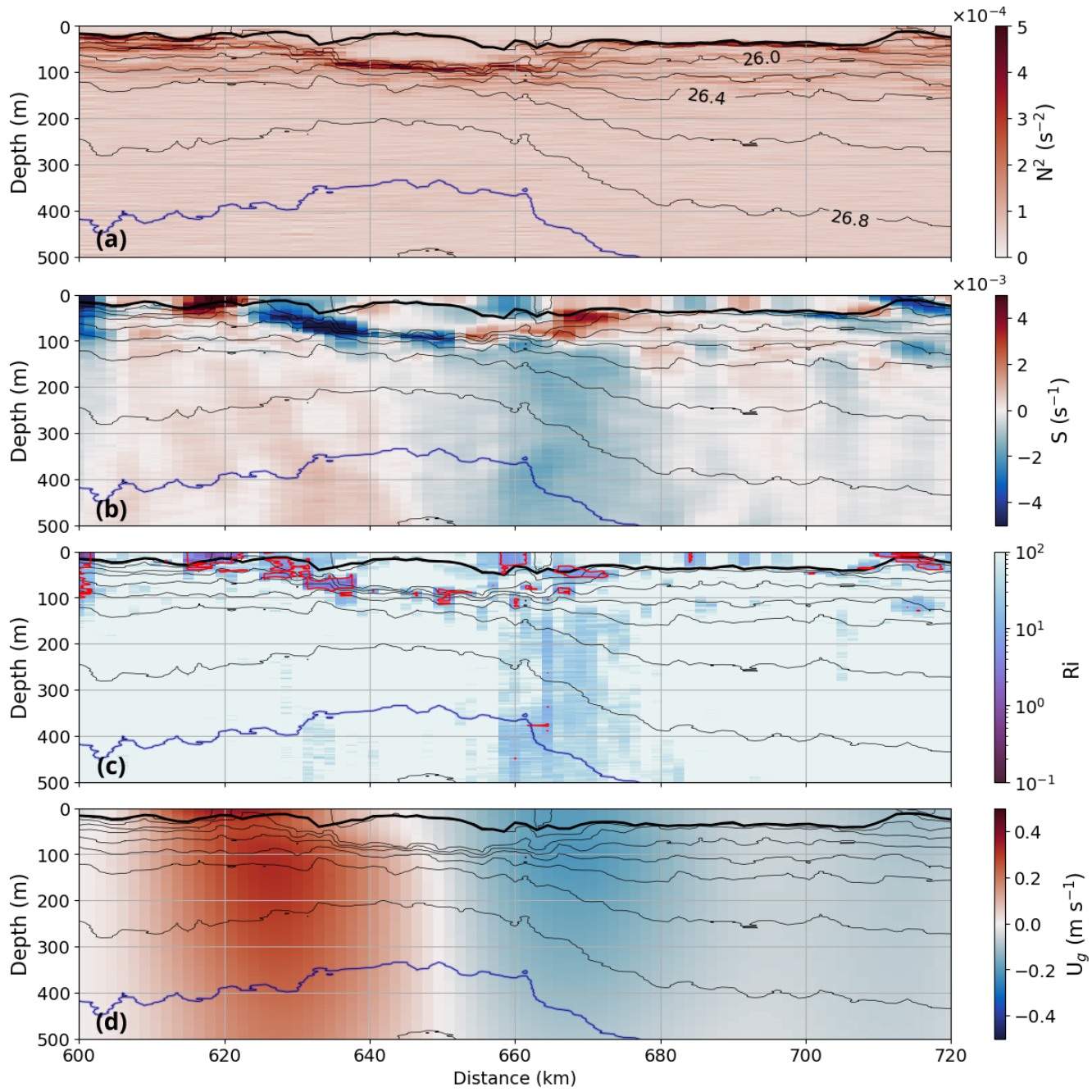
Figure 5. Glider sections of (a) Brunt–Väisälä frequency (N2), (b) vertical shear, (c) Richardson number, with red contour lines indicating $Ri < 10$ and (d) geostrophic velocity. Isopycnals are overlaid using thin black contours, the 27 kg m^{-3} isopycnal is highlighted with a thick blue line and the MLD is depicted with the thick black line.

meters (Fig 4). A reduction in POC within this generally high POC regime ($26 < \sigma < 26.5$ kg m^{-3}) suggests that POC is transported across isopycnals. Once below this shear-influenced region, POC can sink more freely or be redistributed along density surfaces, as demonstrated along the 27.0 kg m^{-3} isopycnal (Fig. 4, blue thick contour). Particles that pass through the pycnocline are eventually trapped by a secondary stratified layer at 400 m depth, corresponding to a density of 27.0 kg m^{-3}, which acts as a barrier to mixing, limiting further vertical transport, leading to localized accumulation of POC between 80 and 400 m depth (Fig. 4).
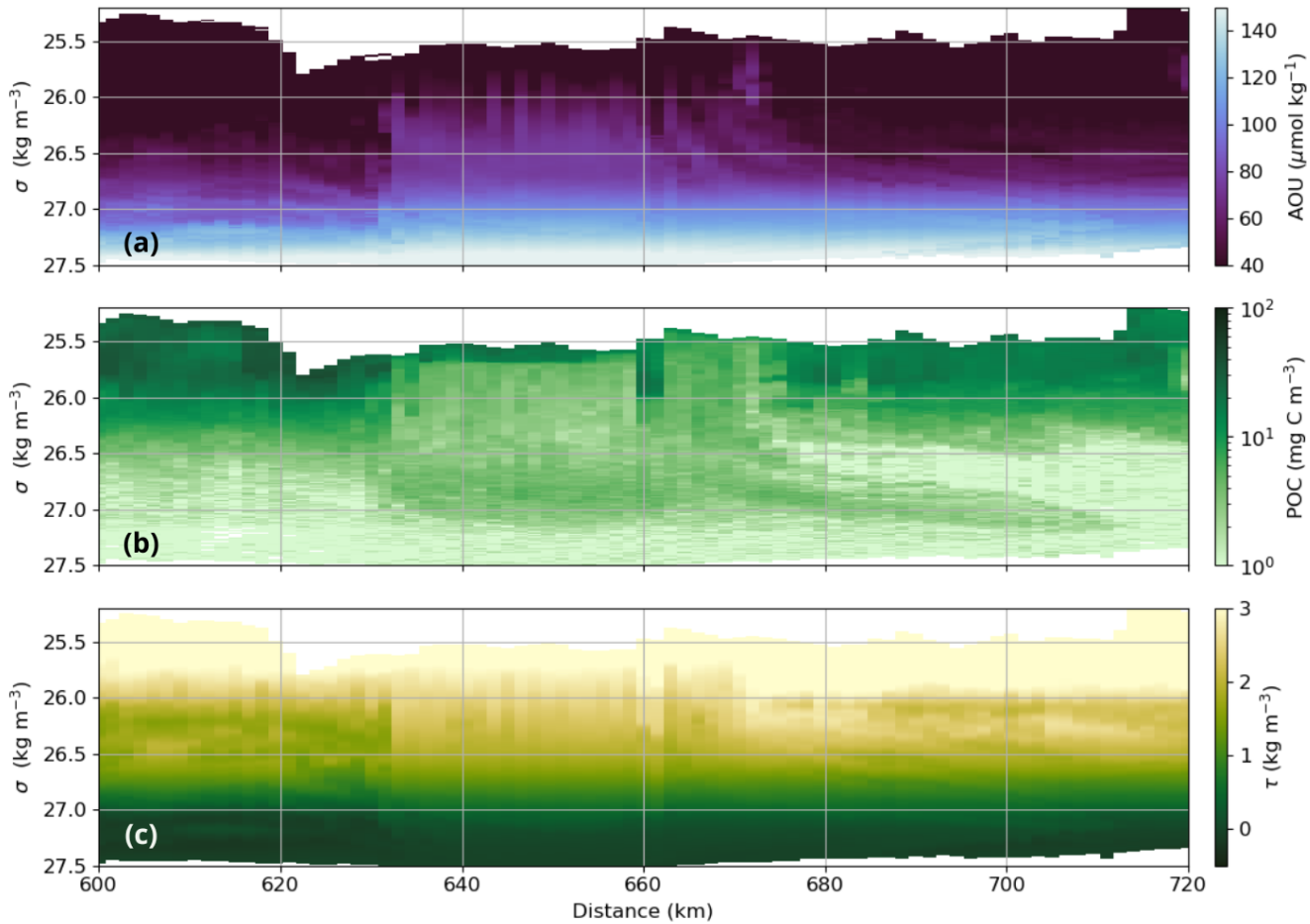
Figure 6. Glider sections showing (a) AOU, (b) POC and (c) Spiciness τ represented in density space.

The cross-isopycnal mixing enhances exchange between the surface boundary layer and the ocean interior between 630 km and 660 km along the gliders path, providing a pathway for particles to move from the surface towards 400 m depth. Elevated AOU values observed below the pycnocline at 80 m depth indicate active remineralization of sinking POC, as microbial decomposition depletes oxygen in subducted waters (Omand et al., 2015). Upward doming isopycnals between 630 - 660 km indicate

upwelling, which could potentially bring nutrients to the surface layer, stimulating photosynthesis and biological activity. However, elevated chlorophyll levels were not observed at the surface, nor was chlorophyll detected at depths below 80 meters. At the same time, POC concentrations remain elevated at depth but are lower in the mixed layer compared to surrounding regions (Fig. 6b), suggesting an enhanced export of POC.

305

Beyond 660 km along the gliders path, the enhanced geostrophic velocity – which extends below 500 m depth (Fig. 5d) – facilitates isopycnal stirring, which contributes to mixing along the density surfaces. As a result, POC is efficiently advected along isopycnals, reaching 800 m in depth (Fig 4c).

310   As discussed in Sec. 3.2, the horizontal buoyancy gradients derived from the glider may be underestimated due to its oblique sampling of ocean fronts. Consequently, the calculated buoyancy gradients, which is used to derive vertical shear and the Richardson number are underestimated. Therefore, the shear instabilities are likely larger than those represented and may have a greater impact on the cross-isopycnal transport than is apparent from the observations.

3.4   Unveiling small-scale drivers of ventilation dynamics

315   Satellite-derived daily average of SLA, SST and FSLE, between May 6 and May 16, 2023 in Fig. 7, combined with glider observations from Fig. 4, reveal the important role of small-scale flow structures and fronts in driving vertical tracer transport. Around 37.5 °S (and between 600 - 630 km), the glider follows a small anticyclonic trajectory, steered by the background depth-averaged current, as indicated by the red arrows in Fig. 7a,d. This small-scale variability in the flow structure is not captured in the satellite images of SLA, due to the low resolution of the AVISO product. However, high variability in temperature and
320   salinity sections suggests that this is a highly dynamic region that can facilitate the interaction and mixing of different water masses. Additionally, elevated EKE and FSLE values were observed in this region (Fig. 1), indicative of enhanced vertical and lateral transport of tracers, including AOU to greater depths (Dove et al., 2021). At intermediate depths (300 - 700 m), low mean AOU values of 80 μmol kg^{-1} were observed, supporting the dynamic interaction that drives vertical transport of surface waters to depth. The glider traverses a high diverging FSLE field at 37.5 °S (Fig. 7c), making this area prone to frontogenesis
325   (d'Ovidio et al., 2004). From 600 - 630 km along the glider's track, the glider is passing through a region with significant SST variability (Fig. 7e) and sharp SST gradients of approximately 0.4 °C km^{-1}, as indicated by the dashed contour lines in (Fig. 7b,e). These surface gradients also extend to depth (Fig. 2a). These subsurface gradients are likely to enhance vertical transport of tracers by driving localized turbulence, facilitating mixing across density layers (Zhu et al., 2024). This process is evident in our observations, where pronounced cross-isopycnal transport occurs near these strong fronts (Fig. 6).
330   Continuing the trajectory from 630 to 660 km along the glider's path, the glider enters a transitional regime where we find elevated AOU values of 120 μmol kg^{-1} averaged between intermediate depths (300 - 700 m) in Fig. 7. The glider samples across sharp SST gradients of approximately 0.6 °C km^{-1}, as indicated by the dashed contour lines in (Fig. 7b), crossing the edges of small-scale cyclones and anticyclones. The path begins at the edge of a strong cyclone and progresses northward, eventually reaching the edge of a smaller secondary cyclone that recently split from the larger cyclone south of 37.5 °S. This
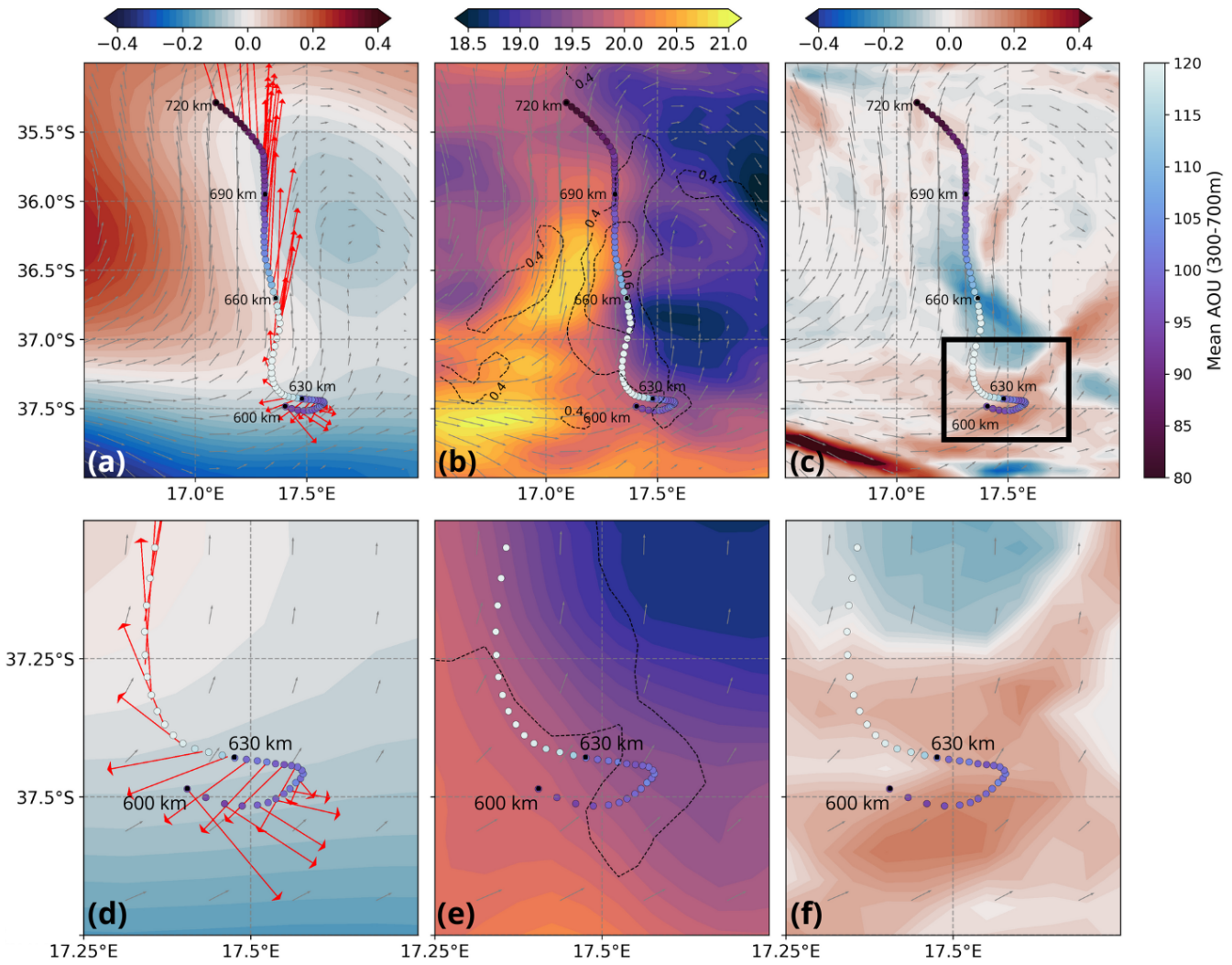
Figure 7. Glider-mission averaged fields (6 May-16 June) of (a) SLA, with red arrows representing the glider depth-averaged current, (b) SST, where the dashed contour lines indicate the temperature gradient and (c) FSLE. Panels (d–f) show zoomed-in views of the black box indicated in panel (c). Geostrophic velocities are represented with the grey vector field. Dots represent the glider trajectory and the color indicates the mean AOU between 300 and 700 m depth.

cross-structure sampling captures vertical transport of tracers across density layers 25.7 to 26.5 kg m^{-3} (Fig. 6), consistent with shear instabilities driving localized diapycnal transport (Fig. 5). In this regime AOU is accumulated at depths near the stratified layer, where oxygen consumption continues, amplifying the processes of respiration and re-mineralization of organic matter.

In contrast, beyond 660 km, the glider primarily follows the edge of a mesoscale eddy and moves along the front. In this regime, vertical tracer transport occurs primarily along tilted isopycnals, rather than through across-isopycnal mixing. The glider is following a path along the edge of the secondary cyclone that is aligned with sharp SST gradients of approximately 0.6 °C km^{-1}, as indicated by the dashed contour lines in (Fig. 7b). Strong geostrophic velocities and elevated depth-averaged current beyond 660 km suggest the glider experiences a transition from a dynamic, high-energy environment of submesoscale turbulence to a more structured, geostrophic regime dominated by advection along density surfaces.

4   Discussion

Previous studies using high-resolution models have highlighted the role of submesoscale processes in driving ventilation in the Cape Basin (Capuano et al., 2018; Schubert et al., 2021). Capuano et al. (2018) emphasized the role of shear instabilities and lateral advection in tracer transport in this region, while Schubert et al. (2021) highlighted how submesoscale processes contribute to stronger Agulhas filaments and the enhancement of shear-edge eddies. These processes lead to more vigorous vertical mixing, facilitating the transport of warm, salty Indian Ocean water into the Atlantic, which is crucial for the ventilation of the AMOC. At the same time, observational studies have mainly focused on mesoscale features in the Cape Basin (Kersalé, M. et al., 2018; Laxenaire et al., 2020), as the detection of submesoscale dynamics requires observations of high spatiotemporal resolution. This study aims to try fill this significant gap by analysing high-resolution glider data in the Cape Basin and provide insights into the meso- to submesoscale mechanisms driving ventilation.

4.1   Drivers of ventilation

The ventilation observed in this study is found to be driven most likely by a combination of shear instabilities, lateral advection and submesoscale fronts (Fig. 8).

Shear instabilities emerge as a significant contributor to vertical mixing, driving diapycnal transport (Fig. 8). In these regions, Richardson numbers approach zero (Fig. 5), and show a reduction in upper ocean stratification. This dynamical regime suggests conditions favorable for enhanced cross-isopycnal mixing and vertical transport, consistent with previous findings on shear instabilities observed in the South China Sea (Tu et al., 2024). Additionally, our observations support the model results of Capuano et al. (2018) in the Cape Basin, confirming that shear instabilities are crucial for vertical transport of tracers in this region.
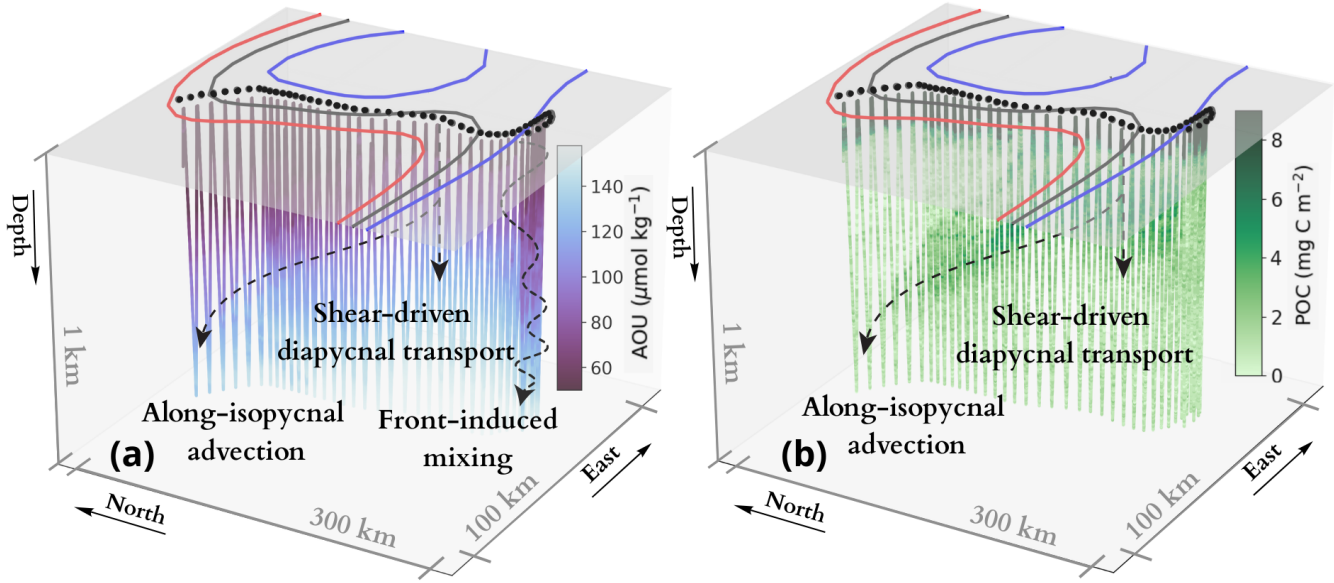
Figure 8. 3D glider transect of (a) AOU and (b) POC. The blue, grey, and red lines represent the Sea Level Anamoly (SLA) respectively (-0.5, 0, 0.5) m.

Lateral advection plays a crucial role in redistributing tracers along isopycnals. Our observations demonstrate how mesoscale eddies facilitate the transport of AOU and POC along isopycnals. This aligns with previous findings, which highlight how mesoscale eddies and standing meanders enhance submesoscale variability, driving a cascade of energy and momentum that strengthens vertical fluxes and tracer exchange (Capuano et al., 2018; Dove et al., 2021; Liu and Tanhua, 2024; Balwada et al., 370 2024). The eddy driven subduction of POC and AOU is concentrated along the edges of these mesoscale eddies, consistent with observations in the North Atlantic (Omand et al., 2015), where dynamic eddy flow fields subduct surface waters rich in non-sinking POC from eddy peripheries into the ocean interior.

In addition, another key mechanism evident in Fig. 8 is the role of fronts in cross-isopycnal transport. These fronts, character-375 ized by strong buoyancy, temperature, and salinity gradients, enhance the vertical flux of tracers. Our observations suggest that the combination of elevated EKE and high buoyancy gradients at these fronts lead to enhanced vertical motions and stronger mixing, enabling AOU to be transported to depth. This observation aligns with previous studies (Siegelman, 2020; Omand et al., 2015), which emphasize the role of submesoscale features in facilitating vertical exchange. The alignment of high FSLE values with strong mixing signatures underscores the importance of surface strain fields in enhancing subduction.

380

In some instances, the glider may cross into a different water mass, making it difficult to precisely locate the source of the ventilated waters. Localized features, such as the subsurface eddy described in Sec. 3.1, can trap and transport recently ventilated waters to depth over small horizontal scales. While this event reflects ventilation associated with the eddy, it is also possible that these waters were ventilated through surface processes in a neighboring region and subsequently advected into the observed area. Therefore, while the vertical transport of tracers appears to be influenced by local mixing and submesoscale dynamics, it is important to consider the possibility that these processes are linked to larger-scale advection and ventilation occurring outside the glider's immediate path.

4.2 Implications

The findings of this study extend beyond local oceanographic dynamics, with the redistribution of heat and carbon impacting both the regional thermohaline structure and potentially large-scale ocean circulation. We show that waters stirred by the oceanic circulation of the Agulhas Current can facilitate the interaction and mixing of water masses that originate from the Indian, Atlantic and Southern Oceans. As ventilated waters are advected downstream along isopycnals, the cumulative anomalies of high POC and low AOU are gradually reduced by remineralization and respiration. While this process is taking place, they can interact with surrounding water masses and contribute to the transport of heat, salt, and tracers toward other parts of the Atlantic, potentially influencing intermediate-depth circulation and branches of the AMOC (Beal et al., 2011; Capuano et al., 2018; Rühs et al., 2022). This exchange contributes to the transport of heat and salt from the Southern Hemisphere to other parts of the Atlantic, and potentially influencing the strength and variability of the AMOC (Beal et al., 2011; Capuano et al., 2018; Rühs et al., 2022). Meso- to submesoscale eddies and fronts are found to enhance lateral and vertical fluxes, driving the downward transport of warm, carbon-rich (high POC) surface waters into the ocean interior. Regions of consistently high FSLE, as shown in Fig. 1c, coincide with elevated EKE and mark persistent hotspots where strong mesoscale stirring and fronts are likely to subduct and ventilate waters, highlighting this particular area (the Cape Basin and particularly just west of the Agulhas Retroflection) as a region of potentially enhanced vertical transport. This has direct consequences for ocean-atmosphere interactions, given that the vertical supplies of heat and carbon can alter air-sea fluxes (Moura et al., 2024).

Similarly, the downward flux of carbon via subduction and subsequent remineralization at depth impacts oceanic carbon sequestration and oxygen consumption, regulating the biological pump and overall carbon cycling. Given that current estimates suggest the biological carbon pump is underestimated (Ricour et al., 2023), a more comprehensive understanding of the fine-scale physical processes driving carbon sequestration, such as those resolved by the glider survey, is needed for closing carbon budgets. Integrating such observational data with high-resolution models will improve estimates of carbon fluxes and enhance predictions of future carbon sequestration in response to climate change. Although this study focuses on the Cape Basin, similar processes might occur in other regions with strong frontal dynamics, such as the Brazil–Malvinas Confluence. These areas remain the focus of active research. Integrating observational datasets with high-resolution models and emerging satellite missions such as SWOT might provide a more holistic view of ventilation and carbon fluxes across the South Atlantic.

5 Conclusions

The results from this study provide new insights into the small-scale dynamics driving ventilation in the Cape Basin and region of the Agulhas Retroflection. Using high-resolution glider data, we were able to map the transport of AOU and identify key processes that enhance vertical and lateral tracer transport.

The glider transects show how AOU is transported from the surface to intermediate depths (300 – 700 m) through lateral stirring and subduction along isopycnals, as well as cross-isopycnal, by shear-driven turbulence and instabilities.

The use of altimetry-derived FSLE revealed that enhanced strain correspond to larger horizontal buoyancy gradients at depth. Such lateral dynamics enhance the subduction of oxygen-rich waters. Additionally, particle backscatter analysis highlight the important role of ocean fronts and shear-driven turbulence facilitating the vertical transport of particles and organic matter, such as POC, towards the ocean interior.

While this study provides valuable insights into both the vertical and horizontal dynamics of this highly energetic region, it has limitations. Firstly, glider-derived buoyancy gradients are underestimated because fronts and filaments are not sampled perpendicularly, especially when the strong currents advect the glider along geostrophic flows. Such underestimation leads to a somewhat incomplete picture of the prevalence and magnitude of shear processes. Future work could address this by incorporating measurements perpendicular to the front, using pairs of gliders sampling in parallel to capture the full horizontal buoyancy gradient, or use high-resolution ship-based hydrographic surveys. Also, future studies would benefit from newly available SSH products incorporating swath altimetry from the SWOT mission, thereby better resolving circulation and strain fields to relate to in situ observations and providing a more complete picture of the dynamics. While this study uniquely highlights the role of small-scale physical processes in driving ventilation and carbon cycling in the Cape Basin, more comprehensive high-resolution observations will help determine if such ventilation regimes are confined to the highly energetic Retroflection region or more widely spread in the Cape Basin and beyond. Future planned winter-time observations will also help elucidate whether deeper MLDs, associated amplified submesoscale instabilities and stronger air-sea fluxes can amplify these ventilation pathways in the Agulhas Current System.

Code and data availability. The Seaglider SG675 data are available at Zenodo (DOI: 10.5281/zenodo.15189207). The CTD data used to calibrate the Seaglider oxygen measurements can be found at Zenodo (DOI: 10.5281/zenodo.15192621). The Global Ocean Gridded L4 Sea Surface Heights and derived variables and the Global Ocean OSTIA Sea Surface Temperature and Sea Ice Analysis are distributed by Copernicus Marine Service. The code used for data analysis and visualization is publicly available at: https://github.com/renskekoets/Ventilation_Cape_Basin

Author contributions. RK conducted the research, performed data analysis, and wrote the manuscript. SS and MdP supervised the project and reviewed and edited the manuscript. KD collaborated on the project and assisted with manuscript revisions.

Competing interests. The authors declare that they have no conflict of interest

Acknowledgements. All in situ ocean data were collected during the QUICCHE project, led by Lisa Beal and Kathleen Donohue, with co-PIs Yueng Lenn, Chris Roman, and Sebastiaan Swart. The project is funded by the US NSF (grants 2148676, 2148677), UK NERC (NE/X006468/1), and the Wallenberg Academy Fellowship of S. Swart (WAF 2015.0186). We thank Johan Edholm, Marcel du Plessis, Isabelle Giddy, Estel Font, and the R/V Revelle (R2302) captain, crew, and technicians for their support in the glider deployments and piloting. This project has received co-funding from the European Union's Horizon Europe ERC Synergy Grant programme under grant agreement No 101118693 - WHIRLS. Views and opinions expressed are however those of the author(s) only and do not necessarily reflect those of the European Union or European Research Council Executive Agency. Neither the European Union nor the granting authority can be held responsible for them.

References

Abarbanel, H., Holm, D., Marsden, J., and Ratiu, T.: Richardson Number Criterion for the Nonlinear Stability of Three-Dimensional Stratified Flow, Physical Review Letters, 52, https://doi.org/10.1103/PhysRevLett.52.2352, 1984.

Balwada, D., Gray, A., Dove, L., and Thompson, A.: Tracer Stirring and Variability in the Antarctic Circumpolar Current Near the Southwest Indian Ridge, Journal of Geophysical Research: Oceans, 129, https://doi.org/10.1029/2023JC019811, 2024.

Beal, L. M., De Ruijter, W. P. M., Biastoch, A., Zahn, R., Cronin, M., Hermes, J., Lutjeharms, J., Quartly, G., Tozuka, T., Baker-Yeboah, S., Bornman, T., Cipollini, P., Dijkstra, H., Hall, I., Park, W., Peeters, F., Penven, P., Ridderinkhof, H., Zinke, J., and 136, S. W. G.: On the role of the Agulhas system in ocean circulation and climate, Nature, 472, 429–436, https://doi.org/10.1038/nature09983, 2011.

Bennett, J. S., Stahr, F. R., Eriksen, C. C., Renken, M. C., Snyder, W. E., and Van Uffelen, L. J.: Assessing Seaglider Model-Based Position Accuracy on an Acoustic Tracking Range, Journal of Atmospheric and Oceanic Technology, 38, 1111–1123, https://doi.org/10.1175/JTECH-D-20-0091.1, online Publication: 08 Jun 2021, Print Publication: 01 Jun 2021, 2021.

Bernat, R. A.: Hydrostatic and Geostrophic Balance, https://rabernat.github.io/intro_to_physical_oceanography/06_hydrostatic_geostrophic.html, accessed: 2024-10-23, 2024.

Berta, M., Ursella, L., Nencioli, F., Doglioli, A. M., Petrenko, A. A., and Cosoli, S.: Surface transport in the Northeastern Adriatic Sea from FSLE analysis of HF radar measurements, Journal of Marine Systems, 224, 103 681, https://doi.org/10.1016/j.csr.2014.01.016, 2022.

Bettencourt, J. H., López, C., Hernández-García, E., Montes, I., Sudre, J., Dewitte, B., Paulmier, A., and Garçon, V.: Boundaries of the Peruvian oxygen minimum zone shaped by coherent mesoscale dynamics, Nature Geoscience, 8, 937–940, https://doi.org/10.1038/ngeo2570, 2015.

Boebel, O., Lutjeharms, J., Schmid, C., Zenk, W., Rossby, T., and Barron, C.: The Cape Cauldron: a regime of turbulent inter-ocean exchange, Deep Sea Research Part II: Topical Studies in Oceanography, 50, 57–86, https://doi.org/10.1016/S0967-0645(02)00379-X, 2003.

Boyd, P. W., Claustre, H., Levy, M., Siegel, D. A., and Weber, T.: Multi-faceted particle pumps drive carbon sequestration in the ocean, Nature, 568, 327–335, https://doi.org/10.1038/s41586-019-1098-2, 2019.

Briggs, N., Perry, M. J., Cetinić, I., Lee, C., D'Asaro, E., Gray, A. M., and Rehm, E.: High-resolution observations of aggregate flux during a sub-polar North Atlantic spring bloom, Deep Sea Research Part I: Oceanographic Research Papers, 58, 1031–1039, https://doi.org/10.1016/j.dsr.2011.07.007, 2011.

Callies, J. and Ferrari, R.: Baroclinic Instability in the Presence of Convection, Journal of Physical Oceanography, 48, 45 – 60, https://doi.org/10.1175/JPO-D-17-0028.1, 2018.

Capuano, T. A., Speich, S., Carton, X., and Blanke, B.: Mesoscale and Submesoscale Processes in the Southeast Atlantic and Their Impact on the Regional Thermohaline Structure, Journal of Geophysical Research: Oceans, 123, 1937–1961, https://doi.org/10.1002/2017JC013396, 2018.

Chen, M. L. and Schofield, O.: Spatial and Seasonal Controls on Eddy Subduction in the Southern Ocean, Geophysical Research Letters, 51, e2024GL109 246, https://doi.org/10.1029/2024GL109246, e2024GL109246 2024GL109246, 2024.

de Boyer Montégut, C., Madec, G., Fischer, A. S., Lazar, A., and Iudicone, D.: Mixed layer depth over the global ocean: An examination of profile data and a profile-based climatology, Journal of Geophysical Research: Oceans, 109, https://doi.org/10.1029/2004JC002378, 2004.

Dove, L. A., Thompson, A. F., Balwada, D., and Gray, A. R.: Observational Evidence of Ventilation Hotspots in the Southern Ocean, Journal of Geophysical Research: Oceans, 126, e2021JC017 178, https://doi.org/10.1029/2021JC017178, 2021.

Dove, L. A., Balwada, D., Thompson, A. F., and Gray, A. R.: Enhanced Ventilation in Energetic Regions of the Antarctic Circumpolar Current, Geophysical Research Letters, 49, e2021GL097 574, https://doi.org/10.1029/2021GL097574, 2022.

d'Ovidio, F., Fernández, V., Hernández-García, E., and López, C.: Mixing structures in the Mediterranean Sea from finite-size Lyapunov exponents, Geophysical Research Letters, 31, https://doi.org/10.1029/2004GL020328, 2004.

du Plessis, M., Swart, S., Ansorge, I. J., Mahadevan, A., and Thompson, A. F.: Southern Ocean Seasonal Restratification Delayed by Submesoscale Wind–Front Interactions, Journal of Physical Oceanography, 49, 1035 – 1053, https://doi.org/10.1175/JPO-D-18-0136.1, 2019.

Dudley B, C., Roland A, d., Michael G, S., Naggar, K. E., and Siwertz, N.: Geographical Variability of the First Baroclinic Rossby Radius of Deformation, Journal of Physical Oceanography, 28, 433 – 460, https://doi.org/10.1175/1520-0485(1998)028<0433:GVOTFB>2.0.CO;2, 1998.

Freilich, M. and Mahadevan, A.: Coherent Pathways for Subduction From the Surface Mixed Layer at Ocean Fronts, Journal of Geophysical Research: Oceans, 126, https://doi.org/10.1029/2020JC017042, 2021.

Fu, Y., Wang, C., Brandt, P., and Greatbatch, R. J.: Interannual Variability of Antarctic Intermediate Water in the Tropical North Atlantic, Journal of Geophysical Research: Oceans, 124, 4044–4057, https://doi.org/10.1029/2018JC014878, 2019.

Garau, B., Ruiz, S., Zhang, W. G., Pascual, A., Heslop, E., Kerfoot, J., and Tintoré, J.: Thermal Lag Correction on Slocum CTD Glider Data, Journal of Atmospheric and Oceanic Technology, 28, 1065 – 1071, https://doi.org/10.1175/JTECH-D-10-05030.1, 2011.

Giulivi, C. F. and Gordon, A. L.: Isopycnal displacements within the Cape Basin thermocline as revealed by the Hydrographic Data Archive, Deep Sea Research Part I: Oceanographic Research Papers, 53, 1285–1300, https://doi.org/10.1016/j.dsr.2006.05.011, 2006.

Gregor, L., Ryan-Keogh, T. J., Nicholson, S.-A., du Plessis, M., Giddy, I., and Swart, S.: GliderTools: A Python Toolbox for Processing Underwater Glider Data, Frontiers in Marine Science, 6, https://doi.org/10.3389/fmars.2019.00738, 2019.

Guo, M., Xing, X., Xiu, P., Dall'Olmo, G., Chen, W., and Chai, F.: Efficient biological carbon export to the mesopelagic ocean induced by submesoscale fronts, Nature Communications, 15, 580, https://doi.org/10.1038/s41467-024-44846-7, 2024.

Ito, T., Follows, M. J., and Boyle, E. A.: Is AOU a good measure of respiration in the oceans?, Geophysical Research Letters, 31, https://doi.org/10.1029/2004GL020900, 2004.

Kersalé, M., Lamont, T., Speich, S., Terre, T., Laxenaire, R., Roberts, M. J., van den Berg, M. A., and Ansorge, I. J.: Moored observations of mesoscale features in the Cape Basin: characteristics and local impacts on water mass distributions, Ocean Science, 14, 923–945, https://doi.org/10.5194/os-14-923-2018, 2018.

Kwon, E. Y., Primeau, F., and Sarmiento, J. L.: The impact of remineralization depth on the air–sea carbon balance, Nature Geoscience, 2, 630–635, https://doi.org/10.1038/ngeo612, 2009.

Lacour, L., Briggs, N., Claustre, H., Ardyna, M., and Dall'Olmo, G.: The Intraseasonal Dynamics of the Mixed Layer Pump in the Subpolar North Atlantic Ocean: A Biogeochemical-Argo Float Approach, Global Biogeochemical Cycles, 33, https://doi.org/10.1029/2018GB005997, 2019.

Laxenaire, R., Speich, S., and Stegner, A.: Agulhas ring heat content and transport in the South Atlantic estimated by combining satellite altimetry and Argo profiling floats data, Journal of Geophysical Research: Oceans, 123, 7794–7809, https://doi.org/10.1029/2019JC015511, 2020.

Leif N, T. and Joyce M, T.: Subduction on the northern and southern flanks of the Gulf Stream, Journal of Physical Oceanography, 40, 429–438, https://doi.org/10.1175/2009JPO4187.1, 2010.

Liu, M. and Tanhua, T.: Water masses in the Atlantic Ocean: water mass ages and ventilation, EGUsphere, 2024, 1–29, https://doi.org/10.5194/egusphere-2024-1362, 2024.

530 Lévy, M., Ferrari, R., Franks, P. J. S., Martin, A. P., and Rivière, P.: Bringing physics to life at the submesoscale, Geophysical Research Letters, 39, https://doi.org/10.1029/2012GL052756, 2012.

Moura, R., de Souza, R. B., Casagrande, F., and da Silva Lindemann, D.: Air–sea heat fluxes variations in the Southern Atlantic Ocean: Present-day and future climate scenarios, International Journal of Climatology, 44, 3136–3153, https://doi.org/10.1002/joc.8517, 2024.

Omand, M., McDonnell, M. J., Oliver, D. S., Henry, W. G., Garabato, R. M., de la Rocha, B. L. D., and Watson, A. J.: Eddy-driven subduction

535 exports particulate organic carbon from the spring bloom, Science, 348, 1037–1041, https://doi.org/10.1126/science.1260062, 2015.

Patmore, R. D., Ferreira, D., Marshall, D. P., du Plessis, M. D., Brearley, J. A., and Swart, S.: Evaluating Existing Ocean Glider Sampling Strategies for Submesoscale Dynamics, Journal of Atmospheric and Oceanic Technology, 41, 647 – 663, https://doi.org/10.1175/JTECH-D-23-0055.1, 2024.

Penven, P., Lutjeharms, J. R. E., and Florenchie, P.: Madagascar: A pacemaker for the Agulhas Current system?, Geophysical Research

540 Letters, 33, https://doi.org/10.1029/2006GL026854, 2006.

Pham, H. T., Verma, V., Sarkar, S., Shcherbina, A. Y., and D'Asaro, E. A.: Rapid Downwelling of Tracer Particles Across the Boundary Layer and Into the Pycnocline at Submesoscale Ocean Fronts, Geophysical Research Letters, 51, e2024GL109674, https://doi.org/10.1029/2024GL109674, e2024GL109674 2024GL109674, 2024.

Reynolds, R. A., Stramski, D., and Mitchell, B. G.: A chlorophyll-dependent semianalytical reflectance model derived from field measure-

545 ments of absorption and backscattering coefficients within the Southern Ocean, Journal of Geophysical Research: Oceans, 106, 7125–7138, https://doi.org/10.1029/1999JC000311, 2001.

Richardson, P. L.: Eddy kinetic energy in the North Atlantic from surface drifters, Journal of Geophysical Research: Oceans, 88, 4355–4367, https://doi.org/10.1029/JC088iC07p04355, 1983.

Ricour, F., Guidi, L., Gehlen, M., DeVries, T., and Legendre, L.: Century-scale carbon sequestration flux throughout the ocean by the

550 biological pump, Nature Geoscience, 16, 1105–1113, https://doi.org/10.1038/s41561-023-01318-9, 2023.

Roullet, G., McWilliams, J. C., Capet, X., and Molemaker, M. J.: Properties of Steady Geostrophic Turbulence with Isopycnal Outcropping, Journal of Physical Oceanography, 42, 18 – 38, https://doi.org/10.1175/JPO-D-11-09.1, 2012.

Ruan, X., Thompson, A. F., Flexas, M. M., and Sprintall, J.: Contribution of topographically generated submesoscale turbulence to Southern Ocean overturning, Nature Geoscience, 10, 840–845, https://doi.org/10.1038/ngeo3053, 2017.

555 Rühs, S., Schmidt, C., Schubert, R., Schulzki, T. G., Schwarzkopf, F. U., Le Bars, D., and Biastoch, A.: Robust estimates for the decadal evolution of Agulhas leakage from the 1960s to the 2010s, Communications Earth & Environment, 3, 318, https://doi.org/10.1038/s43247-022-00643-y, 2022.

Schmid, C., Boebel, O., Zenk, W., Lutjeharms, J., Garzoli, S., Richardson, P., and Barron, C.: Early evolution of an Agulhas Ring, Deep Sea Research Part II: Topical Studies in Oceanography, 50, 141–166, https://doi.org/10.1016/S0967-0645(02)00382-X, inter-ocean exchange

560 around southern Africa, 2003.

Schubert, R., Gula, J., and Biastoch, A.: Submesoscale flows impact Agulhas leakage in ocean simulations, Communications Earth & Environment, 2, 197, https://doi.org/10.1038/s43247-021-00271-y, 2021.

Shcherbina, A. Y., Gregg, M. C., Alford, M. H., and Harcourt, R. R.: Characterizing Thermohaline Intrusions in the North Pacific Subtropical Frontal Zone, Journal of Physical Oceanography, 39, 2735 – 2756, https://doi.org/10.1175/2009JPO4190.1, 2009.

565 Siegelman, L.: Energetic Submesoscale Dynamics in the Ocean Interior, Journal of Physical Oceanography, 50, https://doi.org/10.1175/JPO-D-19-0253.1, 2020.

Siegelman, L., Klein, P., Rivière, P., Thompson, A. F., Torres, H. S., Flexas, M., and Menemenlis, D.: Enhanced upward heat transport at deep submesoscale ocean fronts, Nature Geoscience, 13, 50–55, https://doi.org/10.1038/s41561-019-0489-1, 2020.

Sudre, F., Hernández-Carrasco, I., Mazoyer, C., Sudre, J., Dewitte, B., Garçon, V., and Rossi, V.: An ocean front dataset for the Mediterranean sea and southwest Indian ocean, Scientific Data, 10, 730, https://doi.org/10.1038/s41597-023-02615-z, 2023.

Swart, S., du Plessis, M. D., Thompson, A. F., Biddle, L. C., Giddy, I., Linders, T., Mohrmann, M., and Nicholson, S.-A.: Submesoscale Fronts in the Antarctic Marginal Ice Zone and Their Response to Wind Forcing, Geophysical Research Letters, 47, e2019GL086 649, https://doi.org/10.1029/2019GL086649, e2019GL086649 2019GL086649, 2020.

Thompson, A. F., Lazar, A., Buckingham, C., Garabato, A. C. N., Damerell, G. M., and Heywood, K. J.: Open-Ocean Submesoscale Motions: A Full Seasonal Cycle of Mixed Layer Instabilities from Gliders, Journal of Physical Oceanography, 46, 1285 – 1307, https://doi.org/10.1175/JPO-D-15-0170.1, 2016.

Tu, J., Wu, J., Fan, D., Liu, Z., Zhang, Q., and Smyth, W.: Shear Instability and Turbulent Mixing by Kuroshio Intrusion Into the Changjiang River Plume, Geophysical Research Letters, 51, e2024GL110 957, https://doi.org/10.1029/2024GL110957, e2024GL110957 2024GL110957, 2024.

Wang, B. and Fennel, K.: An Assessment of Vertical Carbon Flux Parameterizations Using Backscatter Data From BGC Argo, Geophysical Research Letters, 50, e2022GL101 220, https://doi.org/10.1029/2022GL101220, e2022GL101220 2022GL101220, 2023.

Wang, T., Suga, T., and Kouketsu, S.: Spiciness anomalies in the upper North Pacific based on Argo observations, Frontiers in Marine Science, 9, https://doi.org/10.3389/fmars.2022.1006042, 2022.

Xia, X., Hong, Y., Du, Y., and Xiu, P.: Three Types of Antarctic Intermediate Water Revealed by a Machine Learning Approach, Geophysical Research Letters, 49, e2022GL099 445, https://doi.org/10.1029/2022GL099445, e2022GL099445 2022GL099445, 2022.

Yu, X., Barkan, R., and Garabato, A. C. N.: Intensification of submesoscale frontogenesis and forward energy cascade driven by upper-ocean convergent flows, Nature Communications, 15, 9214, https://doi.org/10.1038/s41467-024-53551-4, 2024.

Zhang, X., Hu, L., and He, M.-X.: Scattering by pure seawater: Effect of salinity, Opt. Express, 17, 5698–5710, https://doi.org/10.1364/OE.17.005698, 2009.

Zhu, R., Yang, H., Li, M., Chen, Z., Ma, X., Cai, J., and Wu, L.: Observations reveal vertical transport induced by submesoscale front, Scientific Reports, 14, 4407, https://doi.org/10.1038/s41598-024-54940-x, 2024.